1 **The implications of gas slug ascent in a stratified magma for acoustic and**

2 **ground deformation source mechanisms in Strombolian eruptions**

3 Antonio Capponi[*], Stephen J. Lane, Mike R. James

4 *Lancaster Environment Centre, Lancaster University, Lancaster, LA1 4YQ, UK*

5 **now at Department of Earth Sciences, Durham University, Durham, DH1 3LE*

6

7 Corresponding author: Antonio Capponi, Department of Earth Sciences, Durham University,

8 Durham, DH1 3LE, antonio.capponi@durham.ac.uk

9

10   **Abstract**

11   The interpretation of geophysical measurements at active volcanoes is vital for hazard

12   assessment and for understanding fundamental processes such as magma degassing. For

13   Strombolian activity, interpretations are currently underpinned by first-order fluid dynamic

14   models which give relatively straightforward relationships between geophysical signals and gas

15   and magma flow. However, recent petrological and high-speed video evidence has indicated the

16   importance of rheological stratification within the conduit and, here, we show that under these

17   conditions, the straightforward relationships break down. Using laboratory analogue experiments

18   to represent a rheologically-stratified conduit we characterise the distinct variations in the shear

19   stress exerted on the upper sections of the flow tube and in the gas pressures measured above the

20   liquid surface, during different degassing flow configurations. These signals, generated by

21   varying styles of gas ascent, expansion and burst, can reflect field infrasonic measurements and

22   ground motion proximal to a vent. The shear stress signals exhibit timescales and trends in

23   qualitative agreement with the near-vent inflation-deflation cycles identified at Stromboli.

24   Therefore, shear stress along the uppermost conduit may represent a plausible source of near-

25   vent tilt, and conduit shear contributions should be considered in the interpretation of ground

26   deformation, which is usually attributed to pressure sources only. The same range of flow

27   processes can produce different experimental infrasonic waveforms, even for similar masses of

28   gas escape. The experimental data resembled infrasonic waveforms acquired from different vents

29   at Stromboli associated with different eruptive styles. Accurate interpretation of near-vent

30   ground deformation, infrasonic signal and eruptive style therefore requires detailed

31   understanding of: a) spatiotemporal magma rheology in the shallow conduit, and b) shallow

32   conduit geometry, as well as bubble overpressure and volume.

33 **Keyword**

34 Eruption dynamics; slug flow; plugged conduit; volcano infrasonic; ground deformation;

35 analogue experiments

36 **1   Introduction**

37   Strombolian activity is interpreted as the rise, expansion and burst at the magma surface of

38 large gas pockets (*slugs*) (Chouet et al., 1974; Blackburn et al., 1976). This is associated with

39 infrasonic signals, the amplitude of which is used to estimate degassing parameters such as slug

40 volume and overpressure (e.g., Vergniolle and Brandeis, 1996; Ripepe and Marchetti, 2002;

41 James et al., 2009; Lane et al., 2013). At Stromboli, the type volcano for Strombolian-style

42 eruptions, the crater terrace is a constantly evolving system where different vents shift in

43 eruptive style over time scales of hours to years (Harris and Ripepe, 2007). During periods when

44 the activity at a given vent remains constant, the vent may show characteristic infrasonic

45 signatures (e.g., McGreger and Lees, 2004) reflecting diversity of eruption mechanism, with, for

46 a specific conduit geometry, magma viscosity and gas overpressure controlling the transition

47 between passive, transitional or explosive regimes (James et al., 2009; Lane et al. 2013). Ground

48 displacements show a sequence of inflation-deflation cycles associated with pressure variations

49 in the conduit related to slug growth and magma acceleration prior to explosion and following

50 release of the gas-pyroclast mixture to the atmosphere (e.g., Genco and Ripepe, 2010). However,

51 the eruption magnitudes at Stromboli (or, e.g., Sakurajima and Suwanosejima, Japan, Semeru,

52 Indonesia; Iguchi et at., 2008) lead to relatively minor displacements, thus any deformation cycle

53 would likely only be detectable if instruments are deployed in the immediate vicinity of the

54 vents.

55   Interpretation of the geophysical signals associated with Strombolian-style explosive

56   activity has often relied on slug models based on a rheologically uniform, Newtonian low-

57   viscosity magma, consistent with the canonical Strombolian paradigm. Previous laboratory

58   investigations of slug ascent, expansion and burst in single-viscosity systems provided a

59   plausible first-order mechanism for the generation of seismic and acoustic signals (e.g., James et

60   al., 2006; Lane et al., 2013). However, these simplified models cannot explain field and textural

61   evidence (e.g., Lautze and Houghton, 2006; D'Oriano et al., 2011; Gurioli et al., 2014; Capponi

62   et al. 2016b) pointing to the coexistence in the shallower conduit of two rheologically distinct

63   melts, with a higher viscosity magma acting as a plug atop the low-viscosity one.

64   Initial experimental work in a layered system suggested that a plug could increase

65   eruption explosivity and the variability of infrasonic signals (Del Bello et al., 2015). Capponi et

66   al. (2016a) focused on flow organization for slug ascent through a stratified Newtonian magma,

67   revealing three distinct flow configurations depending on the relative slug and plug volumes.

68   Each configuration encompasses different processes: an effective dynamic narrowing and

69   widening of the conduit, instability within the falling liquid films, transient partial blockages of

70   the conduit and slug disruption. These complexities influence slug expansion, burst dynamics

71   and explosion vigour (Del Bello et al., 2015; Capponi et al., 2016a), and thus potentially affect

72   the resulting eruptive style and geophysical signals (e.g., Johnson and Lees, 2000). Lieth and

73   Hort (2016) numerically investigated slug ascent through a magma with variable viscosity filling

74   the conduit. Their results agreed with the experimental and numerical results from Del Bello et

75   al. (2015) and Capponi et al. (2016a) showing that, for plugged conduits, higher plug viscosity

76   caused i) slower ascent of a shorter slug, and ii) higher burst overpressure (Lieth and Hort,

77   2016), and further highlighting the need of a better integration of experimental and numerical

78 methods with field observations linking the eruptive dynamics to the source processes. Although

79 Capponi et al. (2016a) illustrated how a plug may affect the flow organisation, a detailed link

80 between flow processes and pressure variations was missing. Here we provide this link, using

81 experimental and numerical modelling of the source process to present a detailed account on how

82 slug ascent through a rheologically-stratified liquid column produces a variety of pressure

83 changes. This is crucial to 1) constrain the effects of rheological variations on eruption dynamics

84 and resultant geophysical signals, and 2) produce a more detailed picture of the physical

85 conditions in the shallow volcanic conduit that may improve our capability to identify eruptive

86 scenarios and the associated hazards at Strombolian-type volcanoes.

87 **2 Experimental Methods**

88 We used experiments to gain first-order insights into pressure changes generated by slug

89 ascent and burst through rheologically-stratified liquid columns. We injected known gas volumes

90 (V_0) between 2–49 ± 0.1 ml (gas mass M: 0.35–9.0 mg) at the base of a 3-m-high tube filled with

91 a Newtonian silicone oil (*AS100*, viscosity μ = 0.1 Pa s, density ρ = 990 kg/m^3) overlain by

92 variable thickness layer of greater viscosity oil (castor oil, μ = 1 Pa s, ρ = 961 kg/m^3; Fig. 1a)

93 under reduced ambient pressure P_a (3, 1, 0.3 ± 0.1 kPa)), to scale for gas expansion (James et al.,

94 2008). Plug thickness h_p, non-dimensionalised as a function of the tube diameter (D = 0.025 m),

95 ranged between ~2.5–~50 cm (1D–20D) (Capponi et al., 2016a). Slug ascent was mainly

96 controlled by viscous forces within the plug and by inertia with viscous contribution within the

97 silicone oil (Supplementary Material). We measured the pressure within the liquid at the base of

98 the apparatus (P_l); two differential pressure transducers measured pressure changes in the air

99 above the liquid surface with respect to the relatively large volume vacuum chamber connected

100   to the apparatus (ΔP_a). Experiments were imaged at 300 ± 0.1 fps and sensors logged at 5 kHz

101   through LabVIEW, which directly relates individual frames to the pressure data.

102   **3   Flow configurations**

103   The experiments demonstrated three main configurations, bracketed between end-member

104   scenarios of a tube fully filled with either high- or low-viscosity liquid (Fig. 1b, I–V; Capponi et

105   al., 2016a).

106   ██████ **Plug volume significantly greater than slug volume: Configuration 1**

107   As the slug ascended in the low-viscosity oil, gas expansion drove an intrusion of low-

108   viscosity liquid into the plug. The intrusion distributed the plug liquid along the tube wall,

109   forming a viscous annulus around it acting as a dynamic diameter reduction. As the slug nose

110   entered the reduction, the tube area occupied by the slug decreased and its length increased. First,

111   the slug used the intrusion as a pathway through the plug, then moved completely from within

112   the intrusion to within the plug liquid, i.e., the plug fully accommodated the entire slug volume

113   before burst (Figs. 1b-II, 2a C1).

114   ██████ **Plug volume smaller than combined intrusion and slug volumes: Configuration 2**

115   The slug burst with its nose within the plug, whilst its base was in the low-viscosity liquid.

116   Gas expansion drove a greater amount of liquid into the plug compared to C1, and as a result, the

117   annulus enclosed the low-viscosity falling liquid film surrounding the slug body, further

118   reducing the tube area occupied by the slug (Figs. 1b-III, 2a C2).

119   ██████ **Low viscosity intrusion breaches plug: Configuration 3**

120   For sufficiently large gas expansions, the low-viscosity intrusion breached the plug

121   emplacing a layer of low-viscosity liquid above the annulus. The annulus base and top

122 represented a dynamic restriction and widening respectively. As the slug nose passed through the

123 widening, it accelerated causing a rapid drainage of the liquid head above the slug that converged

124 at the top of the annulus. Here, the falling film thickened creating a narrowing neck around the

125 slug. If this closed, the gas flow was temporarily halted and the slug broken into two or more

126 offspring bubbles. Geometry changes led to instability in the falling film around the slug body,

127 creating partial restrictions of the gas escape pathway (Figs. 1b-IV, 2a C3).

128 **4   Experimental results and interpretation**

129   Pressure variations took place during two main phases: (1) as the slug ascended through the

130 liquids (Fig. 2a, I-II), and (2) at burst (Fig. 2a-III).

131 ███ **Slug ascent**

132   In a single-viscosity system, slug elongation led to dynamic support of an increasing

133 mass of oil within the falling liquid film surrounding the slug, leading to decrease in P_l (James et

134 al., 2004; 2008). After burst, the oil drained back to the liquid surface and P_l increased to pre-

135 injection values (e.g., Fig. 2b; Del Bello et al., 2015).

136   In a layered system, plug viscosity hindered gas expansion during slug ascent, retaining

137 gas overpressure. The greater h_p, the less the slug expanded through intruding low-viscosity

138 liquid into the plug (Fig. 2a C2 I-II). Therefore, P_l variations were strongly dependent on M and

139 h_p (i.e., the flow configuration): C3 and C2 showed smaller P_l decreases compared to a single-

140 viscosity scenario, and C1 featured an absolute pressure increase (Fig. 2b). For C1 and constant

141 M, the greatest maximum in P_l occurred when the slug reached the plug base (Fig. 2a C1 II), with

142 a slug length up to ~15% shorter than in the single-viscosity system. For C2, the more the gas

143 expansion drove the liquid intrusion into the plug (Fig. 2a C2 I-II), the faster P_l decreased

144 compared to C1, but the rate of pressure decrease was substantially smaller than the single-

145   viscosity scenario (Fig. 2b). C3 showed a pressure decrease closer to that of the single-viscosity

146   control, but again clearly smaller than during the slug ascent in the low-viscosity liquid. Pressure

147   decrease then accelerated once the intrusion breached the plug, reducing the viscous capping

148   effect and allowing the slug to expand more rapidly, as the low-viscosity liquid layer emplaced

149   above the plug (Figs. 2a C3 I-II, 2b).

150   When the slug nose reached the base of the annulus (Fig. 2a II), it started to ascend

151   through the intrusion. As the slug nose moved from the intrusion to within the plug itself, P_l

152   rapidly started to decrease (Fig. 2b). This was evident for C1, which showed a decreasing

153   pressure ramp whose onset corresponded to the slug nose entering the plug and ended as soon as

154   the plug accommodated the slug base (Fig. 2b). This ramp represented the pressure loss around

155   the slug beginning as the supply of low-viscosity liquid draining into the falling film declined

156   and the tube wall viscously supported an increasing volume of high-viscosity liquid (thicker

157   falling film). The tube cross-sectional area occupied by the slug consequently decreased and the

158   slug length increased. The transition from low- to high-viscosity liquids led to pressure drops

159   ranging between ~95–~3570 Pa, depending on M and h_p. James et al. (2006) observed a similar

160   pressure drop during the passage of slugs through a region of tube narrowing, generated here by

161   the dynamic annulus. Defining an equivalent aspect ratio for the slug size, L', as $L' = L/D =$

162    $4V/\pi D^3$ (with L as bubble length and V a static cylindrical gas volume with the same diameter

163   as the pipe), the overall pressure drop was expressed as

164    $-\Delta P_l \approx \rho g L_i' D_w (1 - A')$ (1),

165   where $L_i^{'}$ is the equivalent aspect ratio of the slug in the lower tube, D_w the diameter of the wider

166   tube (slug in low-viscosity liquid) and A' the ratio of the cross-sectional area of the wider tube to

167   the narrower tube (slug in high-viscosity liquid; equation 6 in James et al., 2006). We measured

168   *L* for calculating *L'* and the radii for the wider and narrower fluid pathways (i.e., tube radius

169   minus the high-viscosity falling liquid film thickness) to obtain *A'* directly from video images.

170   Estimation of $-\Delta P_l$ using equation (1) for 1.1, 4.3 and 9 mg slugs, yields $-\Delta P_l$ of 478, 1520 and

171   2390 Pa respectively. These agree, within expected error, with measured $-\Delta P_l$ values of ~450,

172   ~1340 and ~2800 Pa respectively.

173   Only C1 showed continuously increasing P_l values (Fig. 2b). For C2, the onset of

174   pressure increase was detected only with thick plugs (10*D* and 20*D*), with the slug nose moving

175   into the plug before the accelerated near-surface expansion. Then, as soon as the slug approached

176   the surface, the P_l decrease blended with the faster non-linear pressure drop driven by the very

177   rapid near-surface slug expansion. For C3, the slug transition in the plug was not detected;

178   however, once the low-viscosity intrusion breached the plug, the tube's wall viscously supported

179   the entire plug volume, together with the low-viscosity film surrounding the slug body, as it

180   passed through it, leading to a much greater overall pressure drop compared to equivalent C1–2.

181   Instabilities developed in the falling film around the slug body when the slug nose within the

182   intrusion ascended above the top of the annulus; instabilities propagated downward within the

183   low-viscosity film enclosed within the annulus. The greater *M*, the more these oscillations were

184   pronounced, disrupting the boundary between the two liquids and generating oscillations in P_l

185   with frequencies of ~25–~50 Hz.

186   ██ **Slug burst**

187   As the slug approached the surface, gas expansion accelerated the liquid above it causing

188   a concomitant displacement of the air above the liquid that was detected as an increase in ΔP_a.

189   Simultaneously, liquid flowed into the falling film rapidly decreasing P_l and leaving a meniscus

190   that ruptured at burst. Burst dynamics and ΔP_a changes varied depending on the flow

191   configuration.

4.2.1   Single, low-viscosity system

193   The peak excess pressure, $\Delta P^\wedge_a$, produced by the gas flux relates to M generating it (thus

194   to V_0; Fig. 3a; Lane et al., 2013;): the greater M, the higher $\Delta P^\wedge_a$. For the range of M explored,

195   and $P_a = 1$ kPa, we identified three different behaviours through the dimensionless ratios

196    $\Delta P_b/\Delta P^\wedge_a$, (Lane et al., 2013) and γ, where ΔP_b is a theoretical estimate of the peak dynamic

197   overpressure in the slug at burst (James et al., 2009), and γ is the dimensionless stability index

198   which predicts if a slug will expand in equilibrium with the surrounding liquid and burst

199   passively with negligible dynamic overpressure ($\gamma < 1$) or not ($\gamma > 1$; Del Bello et al., 2012). Lane

200   et al. (2013) identified similar behaviours, classified as passive, transitional and explosive

201   regimes, for the same range of masses and P_a, in a liquid slightly more viscous (0.162 Pa s) and

202   less dense (860 kg/m^3). $\Delta P_b/\Delta P^\wedge_a$ plotted against γ identifies the passive regime for M 0.35-0.17

203   mg ($\gamma < 1$), and the transitional and explosive regimes for 1.1-1.8 mg and 3.1-9 mg ($\gamma > 1$)

204   respectively (Fig. 3b). Visual observation of the ΔP_a waveforms revealed the same regimes, with

205   waveform shapes reflecting increasing gas masses escaping over a constant time-period (Fig. 3c).

206   The overall waveform shapes match, but the peak widths and amplitudes differ: a slower gas

207   expansion, acceleration of the liquid surface and meniscus rupture produce a slow compressional

208   pulse for the passive regime. A narrower pulse, reflecting a more rapid acceleration of the liquid

209   surface, with higher peak amplitude may indicate transitional regime. Highest peak amplitude,

210   narrowest peak and a well-defined coda could be associated with an explosive regime.

211 **4.2.2 Rheologically plugged system**

212   In a layered system, the scaling arguments derived from geometrical considerations

213 (James et al., 2008; Del Bello et al., 2012) cannot be rigorously applied; however, we identified a

214 trend based on the configuration within which the slug burst. For constant h_p, $\Delta P\hat{}_a$ scaled with M

215 (Fig. 4a). For constant M and varying h_p, $\Delta P\hat{}_a$ was a function of flow configuration (Fig. 4b).

216 Smaller M (0.35–1.8 mg), bursting in C3, showed a $\Delta P\hat{}_a$ increase as a function of h_p (1D, 2D,

217 5D). Larger M (3.1–9 mg) showed more variability in $\Delta P\hat{}_a$ within the same configuration and for

218 h_p of 1-2D because the generation of offspring bubbles and partial blockages of the tube lead to a

219 variable impedance of gas escape rate from the parent bubble. For each M, maximum $\Delta P\hat{}_a$ value

220 was usually reached within C2, followed by a $\Delta P\hat{}_a$ decrease for transition to C1 (Fig. 4b). In the

221 absence of C2, the greater peak was usually associated with C1.

222   Figure 5a illustrates the above relationships, showing ΔP_a variations for constant M

223 ascending through a plug of 0D (single-viscosity), 2D, 5D and 20D. A greater $\Delta P\hat{}_a$ characterized

224 all the plugged experiments: C2 clearly showed the greater maximum value, followed by C1 then

225 C3, which featured a longer coda. Differences in waveform shape generated by increasing M

226 identified the passive, transitional and explosive regimes in the single-viscosity system (Fig. 3c);

227 in a layered system, we identified similar classes of waveform shapes, but in signals produced by

228 the same M for different configurations (Fig. 5a).

229   By using both $\Delta P\hat{}_a$ and waveform shape variation, we identified features reflecting different

230 burst dynamics depending on the configuration. C1 and C2 share a similar pulse shape.

231 However, the slower compressional acoustic pulse in C1 resulted from the slower gas expansion

232 and acceleration of the liquid free-surface caused by the slug ascent in a high-viscosity liquid,

233 and the slower rupture of the viscous meniscus and gas release (Fig. 5a). In contrast, the greater

234   ΔP_a increase and the narrowest acoustic pulse width in C2 reflected a rapid acceleration of the

235   liquid surface and a faster disruption of the meniscus and gas release (Fig. 5a). A greater

236   overpressure is expected with a slug surrounded by a thicker falling film, as previous models in

237   single-viscosity systems demonstrated (James et al., 2009; Del Bello et al., 2012). This always

238   occurred in C2, where both a falling film of intruded low-viscosity oil and the viscous annulus

239   enclosing the intrusion surrounded the slug. By contrast, in C1 only the high-viscosity annulus

240   surrounded the slug, resulting in less energetic bursts. C3 showed a longer, lower amplitude

241   signal compared to the other configurations (Fig. 5a). This was due to the combined effect of 1)

242   less over-pressurized slugs compared to C1-2, with gas expansion sufficiently large that the low-

243   viscosity intrusion breaches the plug top, and 2) the gas flow temporarily halted during the slug

244   break-up process, or impeded by partial blockages of the gas escape pathway, leading to

245   progressive gas release and generating secondary pulses and sub-pulses following the main

246   pressure pulse (Fig. 5c). Both secondary pulses and sub-pulses shared similar and reproducible

247   waveforms but showed a progressive decrease in amplitude. To verify that the observed pulses

248   related to the original injected M, we estimated the variations in the mass flux, q, through ΔP_a:

249   $$\Delta P_a = \frac{c}{A}\frac{dM}{dt} = \frac{c}{A}q \qquad\qquad (2),$$

250   where c is sound speed and A the tube cross-sectional area (Lighthill, 1978; Lane et al., 2013).

251   The definite time integral of ΔP_a across the excess pressure peak is proportional to the injected M

252   generating the peak (Lane et al., 2013). When it was possible to visually relate pressure pulses to

253   the main and secondary bursts, integrating around the slug expansion and burst data showed that

254   the sum of the derived M for each pulse was consistent, within error, with the original M value:

255   e.g., derived M of ~6.5 and ~10 mg for initial M of 5.7 and 9 mg respectively. Offspring bubbles

256   may also form from gas loss due to turbulence at the slug base, with consequences on the coda of

257   the burst process (Pering et al., 2016). We didn't observe this experimentally: the offspring

258   bubbles here refer to large secondary bubbles generated by primary slug break-up with

259   consequences on the main burst dynamics.

260   **5   Volcanic implications**

261   The key fluid-dynamic source mechanism responsible for the specific pattern of pressure

262   changes observed within and above the liquid experimentally, and, by similarity, in a volcanic

263   conduit (Lane et al., 2013), is gas expansion driven by reducing pressure during slug ascent. The

264   plug rheology adds further complexities to the expansion process, substantially modifying

265   pressure variations. We identified two distinct phases for the source mechanism: pre-burst and

266   burst.

267   ████**Volcano ground deformation considerations**

268   Pressure change and fluid flow within the conduit before, during and after eruption often

269   generate ground deformation at volcanoes (e.g., Nishimura, 2009). Experimentally, the P_l

270   variations due to the slug ascent, expansion and burst through both a homogeneous liquid and a

271   plugged system began as soon as the slug started to ascend (Fig. 2b). A plug hindered gas

272   expansion and, compared to an unplugged system, relative pressure at the tube base increased

273   until the slug reached the plug base. Experimentally, C1 featured a small absolute pressure

274   increase (Fig. 2b), and 3D computational fluid dynamic (CFD) simulations showed similar basal

275   pressure trends at volcanic-scale (Fig. 6). Following bubble burst, liquid drainage of variable

276   complexity led to return to the starting condition. The viscous shear of liquid against the wall,

277   not measured experimentally, will also contribute to the axial force component of any ground

278   deformation (Chouet et al., 2010), but current models of volcano deformation considered this

279   contribution negligible (e.g., Kawaguchi and Nishimura, 2015).

280   To characterize shear magnitudes at volcano-scale, we carried out CFD simulations using

281   Flow3D, a package optimized for free-surface flows that solves finite difference (or finite

282   volume) approximations to the Navier- Stokes equations over a Cartesian mesh. We considered

283   a slug (V_0 = 158 m^3) ascending in a vertical, rigid conduit (400-m-high, D = 3 m) closed at the

284   base, filled with a 300-m-high magma column modelled either as an incompressible Newtonian

285   fluid of μ = 150 Pa s (single-viscosity), or as a low-viscosity column overlain by a plug of μ = 20

286   kPa s and h_p = 100 m (C1), 60 m (C2) and 30 m (C3) (Supplementary Material; Capponi et al.,

287   2016a). Figure 7 shows the time-height variations of the vertical shear forces (F_s) acting on the

288   conduit (panel I), the sum of the F_s exerted on the conduit wall and the fluid pressure force (F_p)

289   at the conduit base (panel II), and the net force (F_t, panel III).

290   Each configuration led to a different degree of volumetric expansion, triggering different

291   conduit responses to the flow processes. In a single-viscosity system, gas expansion accelerates

292   the liquid above the slug nose, exerting upward-directed shear on the conduit that increases

293   significantly in magnitude as the slug expands rapidly near surface (e.g. James et al 2008). In

294   contrast, the falling film surrounding the slug produces a region of downward shear (Fig. 7a-I).

295   Viscous shear supports an increasing mass of liquid during slug expansion, driving a pressure

296   decrease at the conduit base, thus an upward F_p, compensated by a decreasing F_s (Fig. 7a-II),

297   exerted on the conduit by the falling film, as F_t shows (Fig. 7a-III; James et al., 2008; Chouet et

298   al., 2010; Lieth and Hort, 2016)

299   For C1, the plug restricts gas expansion through exerting upward shear on the conduit of

300   higher magnitude than in the low-viscosity region (Fig. 7b-I). F_p variations reflect a pressure

301   increase below the slug (Fig. 6) generating downward force. As the slug moves into the plug, F_p

302   increases in response to the pressure decrease as the conduit wall viscously supported an

303 increasing volume of high-viscosity liquid (Fig. 7b-II). F_t clearly shows a sequence of downward

304 then upward force, due to i) an overpressurized slug ascending from depth (slug pressure P = ~3

305 $\times 10^6$ Pa) to the plug base (P = ~1.5 $\times 10^6$ Pa) and ii) the dynamic support of mass as the slug

306 moves and expands (P = ~3.3 $\times 10^5$ Pa) into the plug (Fig. 7b-III).

307   For C2, gas expansion initially intrudes the low-viscosity liquid into the plug, exerting a

308 slight upward F_p (and downward F_s, 0–40 s, Fig. 7c-II). This decays slowly as the growing

309 intrusion facilitates gas expansion (40–120 s, P =~2.8 to ~1.2 $\times 10^6$ Pa, Fig. 7c-II). As the slug

310 nose moves into the intrusion, the conduit wall dynamically supports both the falling film

311 intrusion liquid and the viscous annulus surrounding the slug, leading to a downward-traveling

312 pressure reduction below the slug, resulting in an upward F_p (~120 s, Fig. 7c-II). Then, the slug

313 moves from the intrusion into the plug and the rapid near-surface gas expansion increases

314 upward shear in the plug ahead of the slug (P = ~1.2 $\times 10^6$ to ~4.2 $\times 10^5$ Pa, Fig. 7c-I). This cycle

315 generates a sequence of upward-downward-upward force on the conduit (0–40, 40–120, 120–150

316 s, Fig. 7c-III). In C3 we observed a similar, subtler sequence of upward-downward force in F_p

317 (0–40, 40–105 s, Fig. 7d-II); the slug, by intruding the low-viscosity liquid through the plug and

318 emplacing a low-viscosity layer above it, expands more freely (P 40–120 s = ~2.7 to ~1.1 $\times 10^6$

319 Pa, ~3 $\times 10^5$ Pa at burst). However, as the slug passes through the dynamic widening, the rapid

320 draining of the liquid head around the slug nose impinges on the higher-viscosity fluid. This

321 causes a slight change in the forces, further increasing the downward F_p (~105 s, Fig. 7d-II). F_t

322 shows how F_s almost fully compensates F_p, similar to the single-viscosity scenario.

323 Nevertheless, a slight pre-burst downward component is evident (~105 s, Fig. 7d-III),

324 highlighting the presence of pressure instabilities as the slug passes through a shallow dynamic

325 geometry change.

326   Force variations characteristic of each configuration may potentially reflect sequences of

327   conduit inflation-deflation depending on the degree of pressure changes and liquid acceleration

328   through the entire gas expansion process. Figure 7 highlights, for plugged conduits, a significant

329   contribution of shear stress on the conduit in the plug region. We isolated the F_s variations for

330   each configuration, comparing them with the inflation-deflation cycle inferred by tiltmeters at

331   Stromboli (Fig. 8), where Genco and Ripepe (2010) measured near-vent inflation ~200–500 s

332   before Strombolian eruptions, and interpreted this as induced by pressure increase in the conduit

333   due to magma ascent, controlled by slug growth through decompression. Ground inflation rate

334   increased 20–30 s before burst as the near-surface expansion accelerates and, at burst, the

335   conduit contraction following the gas-pyroclast ejection led to a rapid downward tilt (Fig. 8a).

336   Although Genco and Ripepe (2010) explained these cycles only in terms of conduit

337   pressurization-depressurization, for plugged conduits it is possible that both pressure and shear

338   can be plausible source mechanisms for tilt.

339   For a modelled single-viscosity system, shear force contributions noticeably increase ~20 s

340   before burst as the slug rapidly expands near surface (Fig. 8b), giving some waveform similarity

341   to field data. However, magnitudes are small suggesting the shear force contribution may be

342   negligible in low-viscosity magmas. For C1, the same conduit region experiences an upward

343   shear force for ~220 s, due to the ascent from depth of a slug whose expansion is being hindered

344   by the plug viscosity, followed, ~30 s before burst, by a more rapid near-surface acceleration.

345   The overall force magnitude, compared to a single-viscosity system, is also greater (Fig. 8b). For

346   C2, the conduit still experiences the flow process at depth as shallow upward shear force.

347   However, compared to C1, the timeframe is shorter (~100 s) and magnitude larger due to the

348   increased flow rate favoured by a less thick plug (Fig. 8b). The minor amount of viscous material

349   in the magma head at slug burst also favours a more rapid conduit contraction as the gas is

350   released, reflected by a faster decrease of the shear force. C3 shows similar behaviour, with a

351   further increase in the force magnitude ($>10^7$ N) also highlighting variations in the shear force

352   due to the passage of the slug through flow instabilities, possibly generating a further cycle of

353   inflation-deflation preceding the burst (50–100, 110–130 s, Fig. 8b).

354   These force estimates should not be confused with the ones derived by inversion of VLP

355   signals (~10^8 N) for a deeper source and processes originating at depth over the 20–60 second

356   timescale (Chouet et al., 2003, 2008). Our results relate to processes induced by a very shallow

357   source, namely flow of a viscous plug in contact with the conduit wall, potentially responsible

358   only for near-vent tilt. The modelled timescales and trends (Fig. 8) are in plausible qualitative

359   agreement with the near-vent inflation-deflation cycle observed at Stromboli, but previously

360   explained (Genco and Ripepe, 2010) in terms of only pressure change. We suggest that, together

361   with pressure, shear stresses may contribute to the development of a near-vent deformation field,

362   as demonstrated for conduits plugged by an andesitic lava dome where shear stresses mainly

363   seem responsible for deformation (Green et al., 2006). Future studies on the interpretation and

364   quantification of the ground deformation could help to constrain the deformation source

365   mechanism at Stromboli and determine if the forces modelled here are also quantitatively

366   plausible for volcanic conduits and can generate the observed range of near-vent tilt.

367   **Volcano acoustic considerations**

368   Gas expansion and release generated variations in ΔP_a. The time derivative of ΔP_a is a

369   theoretical representation of the acoustic signal in a 3D atmosphere from a 1D source (Lighthill,

370   1978), thus obtaining a synthetic infrasonic waveform to be compared with measured volcanic

371   signals (Supplementary Content; Lane et al., 2013). The qualitative similarity between $d(\Delta P_a)/dt$

372 and Strombolian infrasonic signals demonstrated the plausibility of slug rise and expansion as a

373 first-order fluid-dynamic sources mechanism for infrasonic signals generated by puffing and

374 explosive eruptions at Stromboli (Supplementary Content; Lane et al., 2013).

375      $d(\Delta P_a)/dt$ peak amplitudes in the single-viscosity system scaled with M, particularly for the

376 explosive regime (3.1–9 mg; Fig. 3a, d). In a layered system, flow configuration influences both

377 acoustic amplitude and waveform shape (Fig. 5b) for otherwise similar conditions of M. The

378 comparison of experimental $d(\Delta P_a)/dt$ with the volcanic case requires care, due to both the first-

379 order laboratory approach and path effects during field measurement. The experiments are scaled

380 to the source mechanism of gas expansion, without reproducing the complexities of a natural

381 system (e.g., pyroclasts production and topography). Thus, for comparison we chose infrasonic

382 signals produced at Stromboli from ash-free/-poor eruptions, ejecting pyroclasts to various

383 heights, specific for a given activity at that given vent at a specific time and likely representative

384 of the arrival and burst of a slug at some depth in the conduit (Supplementary Material; Lane et

385 al., 2013).

386   Experimentally, the same M bursting in different configurations produce waveforms

387 resembling infrasonic signals recorded at different vents and different times at Stromboli. For the

388 same gas M (1.1 mg ($V_0 = 6$ ml)) at $P_a = 1$ kPa bursting both in a single low-viscosity system and

389 within C1 (essentially a single high-viscosity system), $d(\Delta P_a)/dt$ showed considerable similarity

390 with the infrasonic waveform of Explosion 95 of Vergniolle et al. (1996), recorded from the

391 eastern vents (Fig. 9a, b). However, the waveform resulting from C1 was the closest match to the

392 natural one (Fig. 9b): the secondary oscillations following the main pulse were better represented

393 and the experimental burst point matched the natural bubble bursting point (Vergniolle et al.,

394 1996). The same M bursting within C2 produced a waveform resembling the ones for the

395 northeast crater zone, NEC (McGreger and Lees, 2004): once again, the main pulse was well

396 reproduced, with some similarities within the following secondary oscillations (Fig. 9c). Finally,

397 the waveform resulting from C3 was remarkably similar to the waveform characterizing the

398 Hornito at the time of measurement (Fig. 9d), matching the main pulse (McGreger and Lees,

399 2004). Furthermore, this synthetic waveform for a plugged system provided a better match for

400 the Hornito than the unplugged system from Lane et al. (2013), with a better match of the

401 secondary oscillations.

402   A 6-ml experimental slug (P_a = 1 kPa) scales to an erupted volcanic gas volume of 95 m^3

403 at atmospheric pressure. Using 3D CFD simulations, we identified possible differences, based

404 purely on visual observations (Capponi et al., 2016a), in burst dynamics resulting from the

405 expansion and burst of such volume for each configuration at volcanic scale. C1 underwent a

406 slow fragmentation of the viscous meniscus above the slug, with few 'pyroclasts' ejected. This

407 compares well to Explosion 95 (eastern vents, Fig. 9b; Vergniolle et al., 1996) described as the

408 arrival and surface burst of bubbles of several sizes, ejecting pyroclasts within the gas jet up to a

409 few metres above the vent. C2 involved a vigorous burst, the fast fragmentation of the meniscus

410 and ejection of 'pyroclasts' to much greater heights above the burst point (these are minimum

411 inertial heights since drag from expanding gas is not modelled). In comparison, the NEC (Fig.

412 9c) produced gas-rich eruptions, 10–20 s long, ash-free/-poor with minor bombs and vertical jets

413 of high velocity pyroclasts reaching heights up to 300 m (McGreger and Lees, 2004). C3

414 produced the ejection of material above the burst point but both their amount and heights were

415 inferior to C2, whilst Hornito produced loud jet-like acoustic noise, with minimal associated

416 ejecta (Fig. 9d; McGreger and Lees, 2004).

417   Thus, the same *M* bursting in different configurations generates laboratory waveforms

418   resembling infrasonic signals typical of a number of specific vent conditions at Stromboli. When

419   scaled to the volcanic case and modelled via CFD simulations, we observed distinct burst

420   dynamics similar to those observed from vents at the time they showed a given activity at that

421   given vent. Therefore, slug escape through a rheologically-stratified fluid can provide a plausible

422   source mechanism for infrasonic signals at Stromboli and help explain the variable explosive

423   style observed. Accurate interpretation of infrasonic signals requires detailed understanding of:

424   a) spatiotemporal magma rheology in the shallow conduit, and b) shallow conduit geometry, as

425   well as bubble overpressure and volume (e.g., Vergniolle and Brandeis, 1996; Lane et al., 2013).

426   The same range of gas volumes, depending on plug properties, can lead to different

427   configurations promoting different eruptive styles (Capponi et al., 2016a) and, as the pressure

428   and force variations demonstrate, modifying the geophysical signals accordingly. Thus, the

429   eruptive style variability inferred by infrasonic signals for each vent cannot be attributed

430   exclusively to variation in slug metrics, but may depend entirely on variations in the magmatic

431   condition (i.e., flow configurations) and supply rate of slugs, which may control the

432   configuration transition and vent geometry.

433   Slug break-up and consequent partial restrictions of the slug path, characterizing C3 (Fig.

434   2a), led, experimentally, to highly variable gas release rates (Fig. 5c) with the main strong

435   compressional pulse followed by secondary pulses (burst of offspring bubbles) and sub-pluses

436   (transient restriction of gas escape). The secondary pulses showed a gradual decrease in acoustic

437   amplitude, mirroring a decrease in the overpressure within each gas pocket bursting at the

438   surface; sub-pulse amplitude is always lower than that of secondary pulses. CFD simulations

439   illustrated the same flow processes at volcanic-scale (Capponi et al., 2016a). Linking flow

440   process to acoustic signal suggests that a greater frequency of pulses and sub-pulses is favoured

441   by lower viscosity of the underlying magma. Assuming pyroclast velocity is related to gas

442   overpressure, the successive release of increasingly less overpressured gas pockets would result

443   in eruption modulation characterized by decaying pyroclast ejection pulses; this trend has been

444   observed volcanically with high-speed visible and thermal videos (Harris et al. 2012; Taddeucci

445   et al. 2012). Second-order velocity fluctuations between volcanically observed main ejection

446   pulses (Gaudin et al., 2014) could relate to the experimental pressure fluctuations generated by

447   the partial restriction of the gas escape pathway observed theoretically and experimentally. The

448   experimental acoustic signal ($d(\Delta P_a)/dt$) also showed a complex waveform (Fig. 5d), with

449   multiple pulses of variable amplitude, interspaced by high-frequency oscillations. These are the

450   most heterogeneous waveforms generated, and with longest duration, reflecting a longer volume-

451   discharge process. At Stromboli, the South-West vents often produced longer and more complex

452   infrasonic signals, with a low-amplitude compressional pulse followed a longer coda, modelled

453   as the bursting of smaller bubbles at the surface or longer mass discharge processes (McGreger

454   and Lees, 2004; Ripepe et al. 2008). Thus, the slug break-up mechanism, together with the

455   generation of transient partial blockages of the conduit that both require a rheological plug, are

456   likely to be operative at Stromboli and are a plausible mechanism for the longer and more

457   complex eruptions that generate distinct infrasonic signals and eruption styles.

458

459   **███ Signal coupling**

460   The fluid-flow processes that form acoustic signal source mechanisms within each

461   configuration (Figs. 5, 9) are the same as the source mechanisms for ground deformation through

462   pressure and shear force (Figs. 7, 8). This raises the possibility of coupled interpretation of

463   acoustic and near-vent ground deformation signals in terms of a single fluid-dynamic process.

464   We cannot make direct comparison here because (a) acoustic signals were not modelled in the

465   CFD simulations, and (b) shear forces were not measured experimentally. Experimental liquid

466   pressure changes occurred on a timescale of ~5 s (Fig. 2b). Natural acoustic signals are ~10

467   times the period of the experimental system (Fig. 9c, d). Taking these factors to approximate the

468   coupled relationship between experimental and natural conduit forces gives a timescale of 50 s

469   for a measurable ground deformation signal. This is of similar magnitude to the tilt timescale

470   recorded by Genco and Ripepe (2010; Fig. 8a) and provides tentative evidence of coupling

471   between near-vent ground deformation and infrasonic acoustic signals both generated by shallow

472   conduit fluid dynamics.

473   ▉▉▉▉**Interaction between plug formation and slug generation timescales**

474   The equilibrium between development timescales of rheological stratification at the top

475   of the magma column and disruption timescales by gas slug ascent (Fig. 10a) can be perturbed as

476   slugs start to form and rise more frequently. Experiments suggest that a path of low-viscosity

477   magma within the plug may be created over time and kept open (i.e., rapid transition from C1-2

478   to C3; Fig. 10). If such activity remains steady in time generating a semi-permanent path through

479   the plug, then a circulatory system may develop. The continuous and frequent arrival of slugs

480   could favour a constant low-viscosity magma influx in the central part of the conduit, while the

481   degassed dense material comprising the viscous annulus sinks at depth, descending in the region

482   surrounding the low-viscosity intrusion and clearing the shallower part of the conduit over time.

483   Conversely, a lower frequency of slug formation would favour the generation of a stable plug,

484   whose thickness and, thus, flow configuration, will depend on time for magma to cool and degas

485   in-between explosions (Fig. 10a, b). Thus, for volcanoes with constantly active multiple vents

486   (e.g., Stromboli and Yasur), each vent may be characterized by an open path through the plug to

487   the surface or by variable h_p, producing different eruptive styles and, ultimately, distinct

488   infrasonic signatures depending on the timescale of slug formation interacting with the timescale

489   of rheological stratification. For a highly dynamic system such as Stromboli, any change in the

490   timescale of slug and plug formation, as well as in slug size, may lead to an abrupt shift in gas

491   escape regime and, therefore, eruptive style and geophysical signals at a given vent.

492   **6   Conclusions**

493   Gas slug ascent through a rheologically-stratified liquid column produced a variety of

494   pressure changes, with magnitudes strongly dependent on the floe configuration in which the

495   slug expanded and burst. Each configuration induces distinct shear stresses variations on the

496   conduit, possibly contributing to the near-vent inflation-deflation cycles identified at Stromboli.

497   Timescales and trends of variation in the conduit forces correlate qualitatively with field data.

498   Therefore, for the interpretation of tilt in a plugged conduit, the contribution of shear stress

499   should be considered as a source for ground deformation, together with the pressure source.

500   The same gas mass bursting in each configuration produced distinct peak amplitudes and

501   waveform shapes, reflecting different burst processes. Similarities between infrasonic

502   measurements from different vents at Stromboli and synthetic waveforms for each configuration

503   demonstrated that infrasonic signals can be interpreted in terms of slugs expanding and bursting

504   through a plug. Each vent at Stromboli showing a distinct infrasonic signature may mirror

505   different rheological conditions, with the slug size and repeat frequency dictating the

506   configuration transition. High-frequency slug ascents should favour the formation of a pathway

507   within the plug, producing longer and more complex eruptions featuring multiple burst and

508   pressure fluctuations, as both natural and experimental infrasonic signals showed. A smaller slug

509   frequency may allow the formation of a uniform plug, for which thickness and, thus,

510   configuration and associated infrasonic signal depend on the time interval between each slug or

511   on variations in slug size.

512   **7   Acknowledgments**

517 **References**

518 Blackburn, E.A., Wilson, L., and Sparks, R.S.J., 1976, Mechanisms and dynamics of strombolian

519 activity. Journal of the Geological Society, v. 132, no. 4, p. 429–440, doi:

520 10.1144/gsjgs.132.4.0429.

521 Capponi, A., James, M.R., and Lane, S.J., 2016a, Gas slug ascent in a stratified magma:

522 Implications of flow organisation and instability for Strombolian eruption dynamics. Earth

523 Planet. Sci. Lett., http://dx.doi.org/10.1016/j.epsl.2015.12.028.

524 Capponi, A., Taddeucci, J., Scarlato, P., and Palladino D.M., 2016b, Recycled ejecta modulating

525 Strombolian explosions. Bull. Volcanol., doi: 10.1007/s00445-016-1001-z.

526 Chouet, B., Hamisevicz, N., and Mcgetchin, T.R., 1974, Photoballistics of Volcanic Jet Activity

527 at Stromboli, Italy. J. Geophys. Res., v. 79, no. 32, p. 4961–4976.

528 Chouet, B., P. Dawson, Ohminato, T., Martini, M., Saccorotti, G., Giudicepietro, F., De Luca,

529 G., Milana, G., and Scarpa, R., 2003, Source mechanisms of explosions at Stromboli Volcano,

530 Italy, determined from moment-tensor inversions of very-long-period data. J. Geophys. Res.,

531 108(B1), 2019, doi:10.1029/2002JB001919.

532 Chouet, B., Dawson, P., Martini, M., 2008, Shallow-conduit dynamics at Stromboli Volcano,

533 Italy, imaged from waveform inversions. In: Lane, S.J., Gilbert, J.S. (Eds.), Fluid Motions in

534 Volcanic Conduits: A Source of Seismic and Acoustic Signals: Geol. Soc., London, Special

535 Publications, 307, pp. 57–84.

536   Chouet, B.A., Dawson, P.B., James, M.R., Lane, S.J., 2010, Seismic source mechanism of

537   degassing bursts at Kilauea Volcano, Hawaii: Results from waveform inversion in the 10–50 s

538   band. J. Geophys. Res., 115:B09311, doi:10.1029/2009JB006661.

539   D'Oriano, C., Bertagnini, A., and Pompilio, M., 2011, Ash erupted during normal activity at

540   Stromboli (Aeolian Islands, Italy) raises questions on how the feeding system works. Bull.

541   Volcanol., v. 73, no. 5, p. 471–477, doi: 10.1007/s00445-010-0425-0.

542   Del Bello, E., Llewellin, E.W., Taddeucci, J., Scarlato, P., and Lane, S.J., 2012, An analytical

543   model for gas overpressure in slug-driven explosions: Insights into Strombolian volcanic

544   eruptions. J. Geophys. Res., v. 117, no. B2, p. B02206, doi: 10.1029/2011JB008747.

545   Del Bello, E., Lane, S.J., James, M.R., Llewellin, E.W., Taddeucci, J., Scarlato, P., Capponi, A.,

546   2015, Viscous plugging can enhance and modulate explosivity of strombolian eruptions. Earth

547   Planet. Sci. Lett., v. 423, 1 August 2015, p. 210-218, ISSN 0012-821X,

548   http://dx.doi.org/10.1016/j.epsl.2015.04.034.

549   Gaudin, D., Taddeucci, J., Scarlato, P., Moroni, M., Freda, C., Gaeta, M., and Palladino, D.M.,

550   2014, Pyroclast Tracking Velocimetry illuminates bomb ejection and explosion dynamics at

551   Stromboli (Italy) and Yasur (Vanuatu) volcanoes. J. Geophys. Res., v. 119, no. 7, p. 5384–5397,

552   doi: 10.1002/2014JB011096.

553   Genco, R., and Ripepe, M., 2010, Inflation-deflation cycles revealed by tilt and seismic records

554   at Stromboli volcano, Geophys. Res. Lett., v. 37, L12302, doi: 10.1029/2010GL042925.

555   Green, D.N., Neuberg, J., Cayol, V., 2006, Shear stress along the conduit wall as a plausible

556   source of tilt at Soufriere Hills volcano, Montserrat, Geophys. Res. Lett., v. 33, L10306,

557   doi:10.1029/2006GL025890.

558   Gurioli, L., Colò, L., Bollasina, A.J., Harris, A.J.L., Whittington, A., and Ripepe, M., 2014,

559   Dynamics of strombolian explosions: inferences from field and laboratory studies of erupted

560   bombs from Stromboli volcano. J. Geophys. Res., v. 119, 319–345, doi:10.1002/2013JB010355.

561   Harris, A., and M. Ripepe (2007), Temperature and dynamics of degassing at Stromboli, J.

562   Geophys. Res., 112, B03205, doi:10.1029/2006JB004393.

563   Harris, A.J.L., Ripepe, M., Hughes, E.A., 2012, Detailed analysis of particle launch velocities,

564   size distributions and gas densities during normal explosions at Stromboli, J. Volcanol. Geoth.

565   Res., doi:10.1016/j.jvolgeores.2012.02.012.

566   Iguchi, M., Yakiwara, H., Tameguri, T., Hendrasto, M., Hirabayahi, J., 2008, Mechanism of

567   explosive eruption revealed by geophysical observations at the Sakurajima, Suwanosejima and

568   Semeru volcanoes J. Volcanol. Geoth. Res., doi:10.1016/j.jvolgeores.2007.10.010.

569   James, M.R., Lane, S.J., and Chouet, B.A., 2006, Gas slug ascent through changes in conduit

570   diameter: Laboratory insights into a volcano-seismic source process in low-viscosity magmas. J.

571   Geophys. Res., v. 111, no. B5, p. B05201, doi: 10.1029/2005JB003718.

572   James, M.R., Lane, S.J., and Corder, S.B., 2008, Modelling the rapid near-surface expansion of

573   gas slugs in low viscosity magmas. Geological Society, London, Special Publications, v. 307, no.

574   1, p. 147–167, doi: 10.1144/SP307.9.

575   James, M.R., Lane, S.J., Wilson, L., and Corder, S.B., 2009, Degassing at low magma-viscosity

576   volcanoes: Quantifying the transition between passive bubble-burst and Strombolian eruption: J.

577   Volcanol. Geotherm. Res., v. 180, no. 2-4, p. 81–88, doi: 10.1016/j.jvolgeores.2008.09.002.

578   Johnson, J., Lees, J., 2000, Plugs and chugs-seismic and acoustic observations of degassing

579   explosions at Karymsky, Russia and Sangay, Ecuador. J. Volcanol. Geotherm. Res.101, 67–82.

580   Kawaguchi, R.,. Nishimura, T., 2015, Numerical investigation of temporal changes in volcanic

581   deformation caused by a gas slug ascent in the conduit. J. Volcanol. Geother. Res., 302:1-10,

582   doi:10.1016/j.jvolgeores.2015.06.002.

583   Lane, S.J., James, M.R., and Corder, S.B., 2013, Volcano infrasonic signals and magma

584   degassing: First-order experimental insights and application to Stromboli. Earth Planet. Sci.

585   Lett., v. 377-378, p. 169–179, doi: 10.1016/j.epsl.2013.06.048.

586   Lautze, N.C., and Houghton, B.F., 2006, Linking variable explosion style and magma textures

587   during 2002 at Stromboli volcano, Italy. Bull. Volcanol., v. 69, no. 4, p. 445–460, doi:

588   10.1007/s00445-006-0086-1.

589   von der Lieth, J., and Hort, M., 2016, Slug ascent and associated stresses during strombolian

590   activity with non-Newtonian rheology, J. Geophys. Res. Solid Earth, 121, 4923–4942,

591   doi:10.1002/2015JB012683.

592   Lighthill, M.J., 1978, Waves in Fluids, Cambridge University Press, Cambridge, UK,

593   ISBN0521010454, 2001, reissue.

594 McGreger, A.D., and Lees, J.M., 2004, Vent discrimination at Stromboli volcano, Italy. J.

595 Volcanol. Geotherm. Res., v. 137, 169–185, doi:10.1016/j.jvolgeores.2004.05.007.

596 Nishimura, T., Ground deformation caused by magma ascent in an open conduit. J. Volcanol.

597 Geotherm. Res., v. 187, 178–192, doi:10.1016/j.jvolgeores.2009.09.001

598 Ripepe, M., and Marchetti, E., 2002, Array tracking of infrasonic sources at Stromboli volcano.

599 Geophys. Res. Lett. 29 (22), 2076, doi:10.1029/2002GL015452

600 Ripepe, M., Delle Donne, D., Harris, A., Marchetti, E., and Ulivieri, G., 2008, Dynamics of

601 Strombolian activity. The Stromboli Volcano: An Integrated Study of the 2002-2003 Eruption,

602 39-48.

603 Taddeucci, J., Alatorre-Ibargüengoitia, M.A., Moroni, M., Tornetta, L., Capponi, A., Scarlato, P.,

604 Dingwell, D.B., De Rita, D., 2012, Physical parameterization of Strombolian eruptions via

605 experimentally-validated modelling of high-speed observations. Geophys. Res. Lett.,

606 doi:10.1029/2012GL052772.

607 Vergniolle, S., and Brandeis, G., 1996, Strombolian explosions 1. A large bubble breaking at the

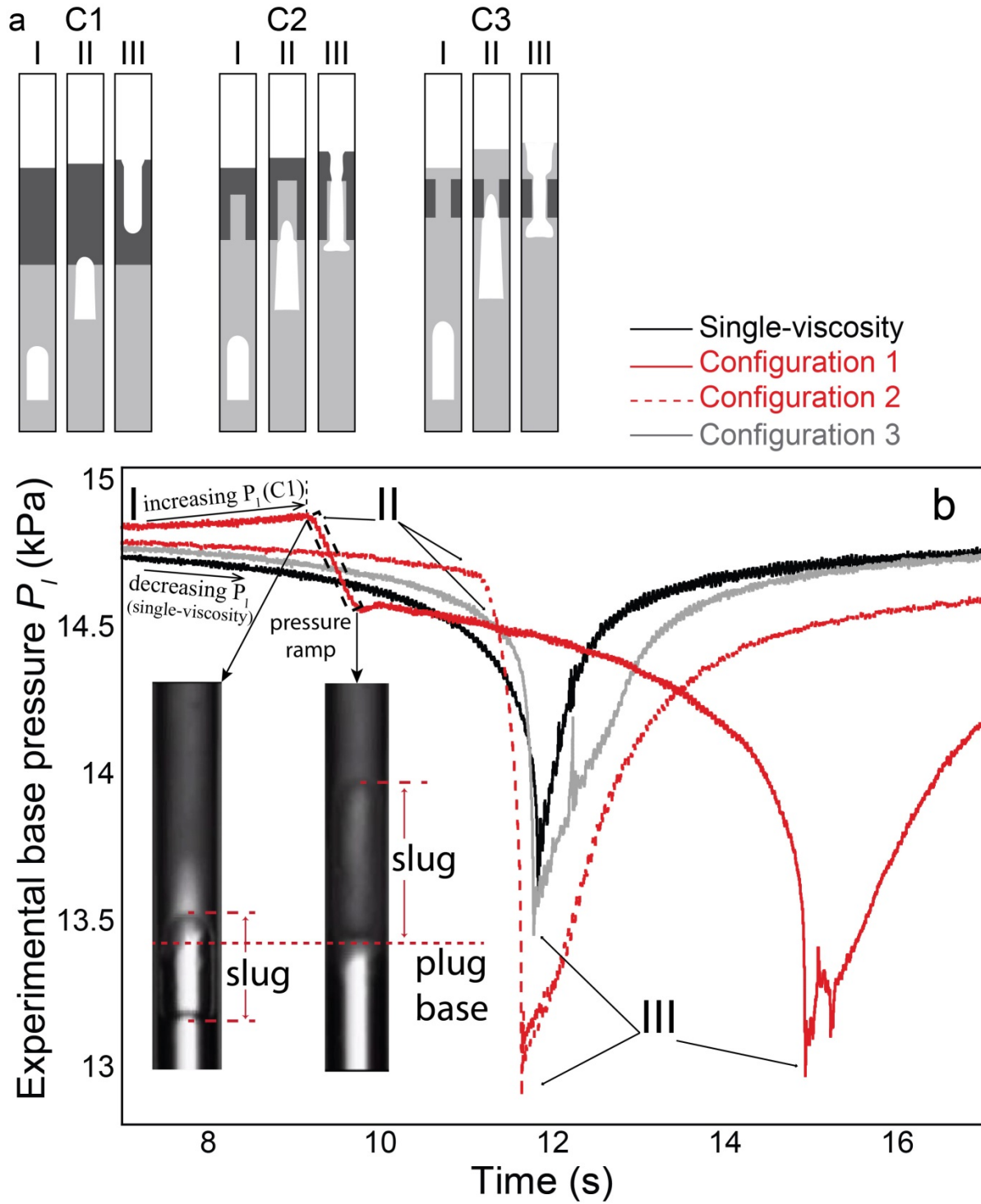608 surface of a lava column as a source of sound. J. Geophys. Res., v. 101, no. B9, p. 433–447.

609 Vergniolle, S., Brandeis, G., and Mareschal, J.C., 1996, Strombolian explosions 2. Eruption

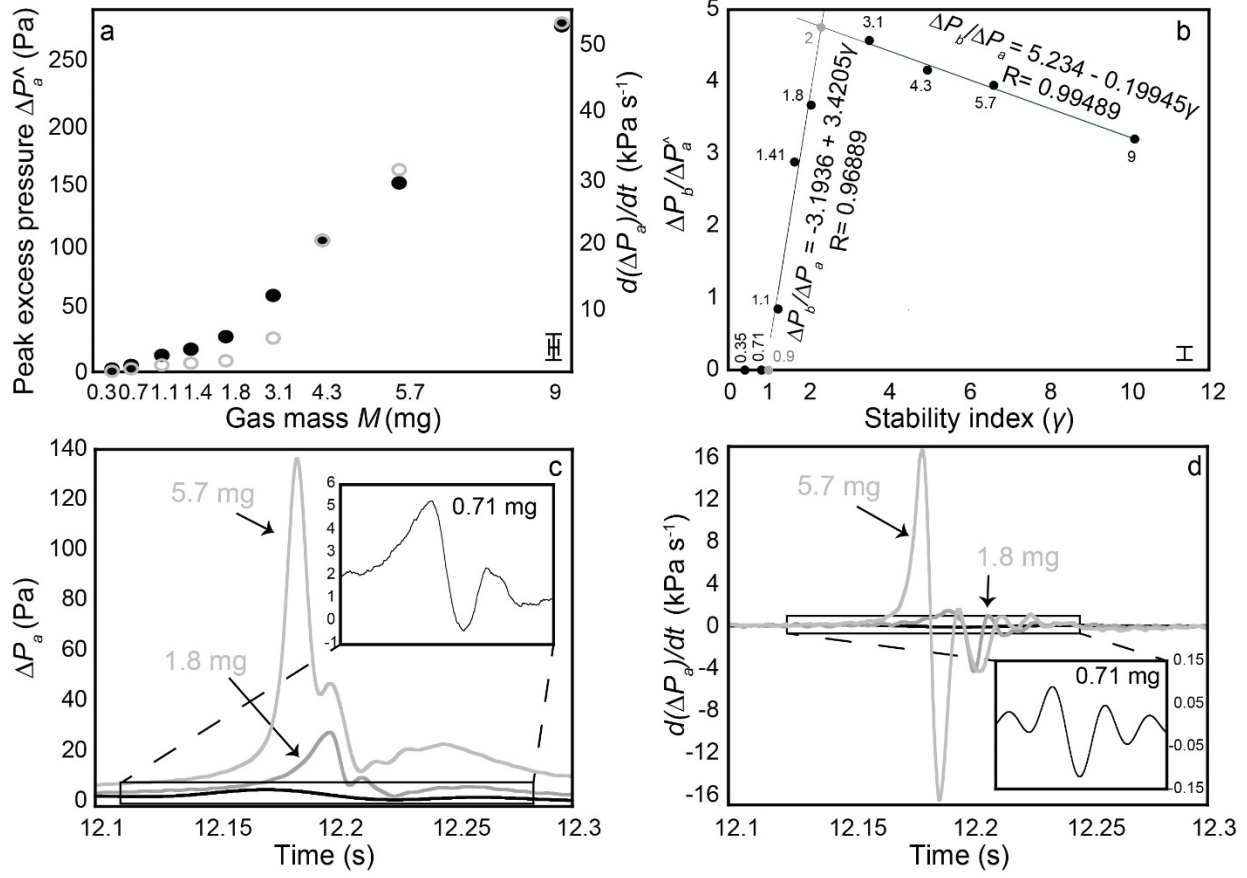610 dynamics determined from acoustic measurements. J. Geophys. Res., v. 101, no. B9, p. 449-466.
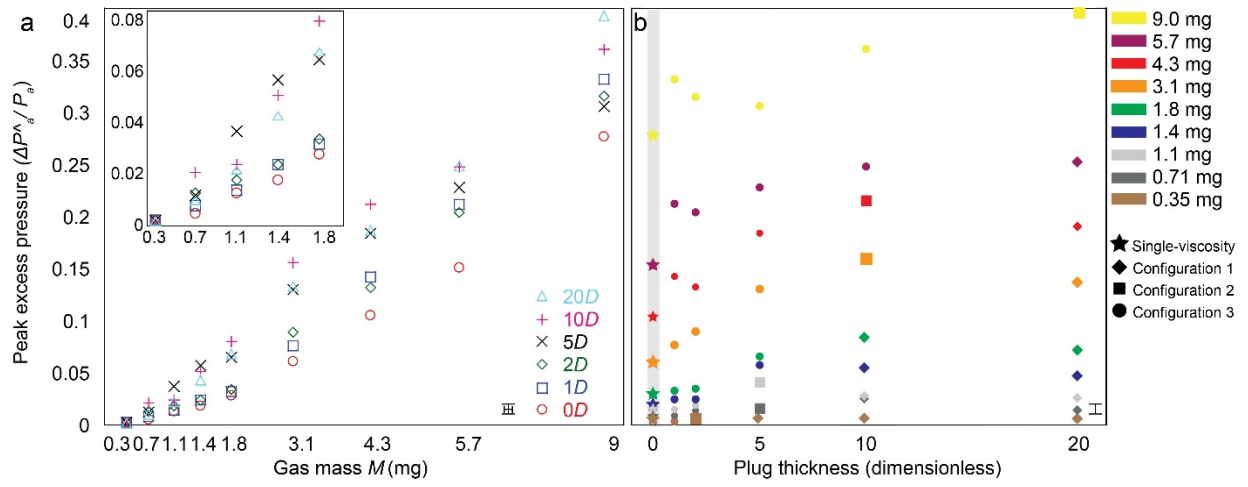
611

612 **Figures**
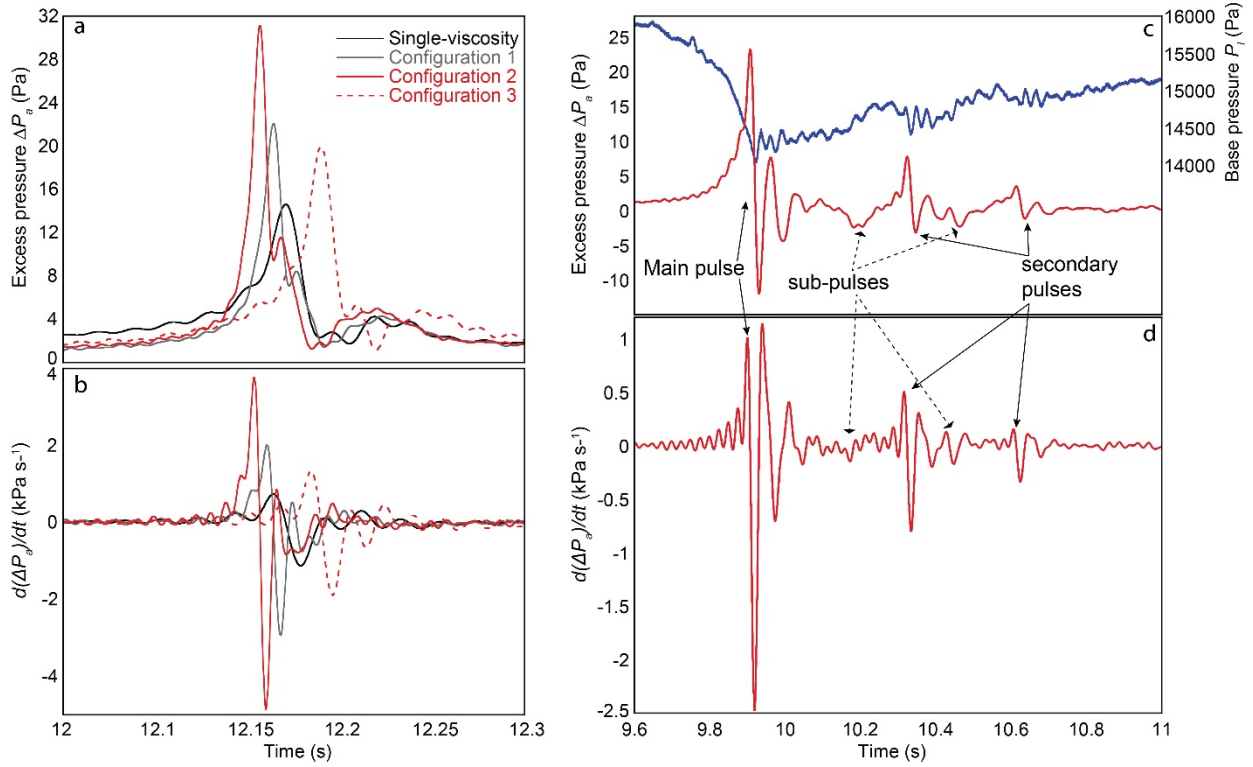
613 **Figure 1**

614

615

616   **Figure 2**
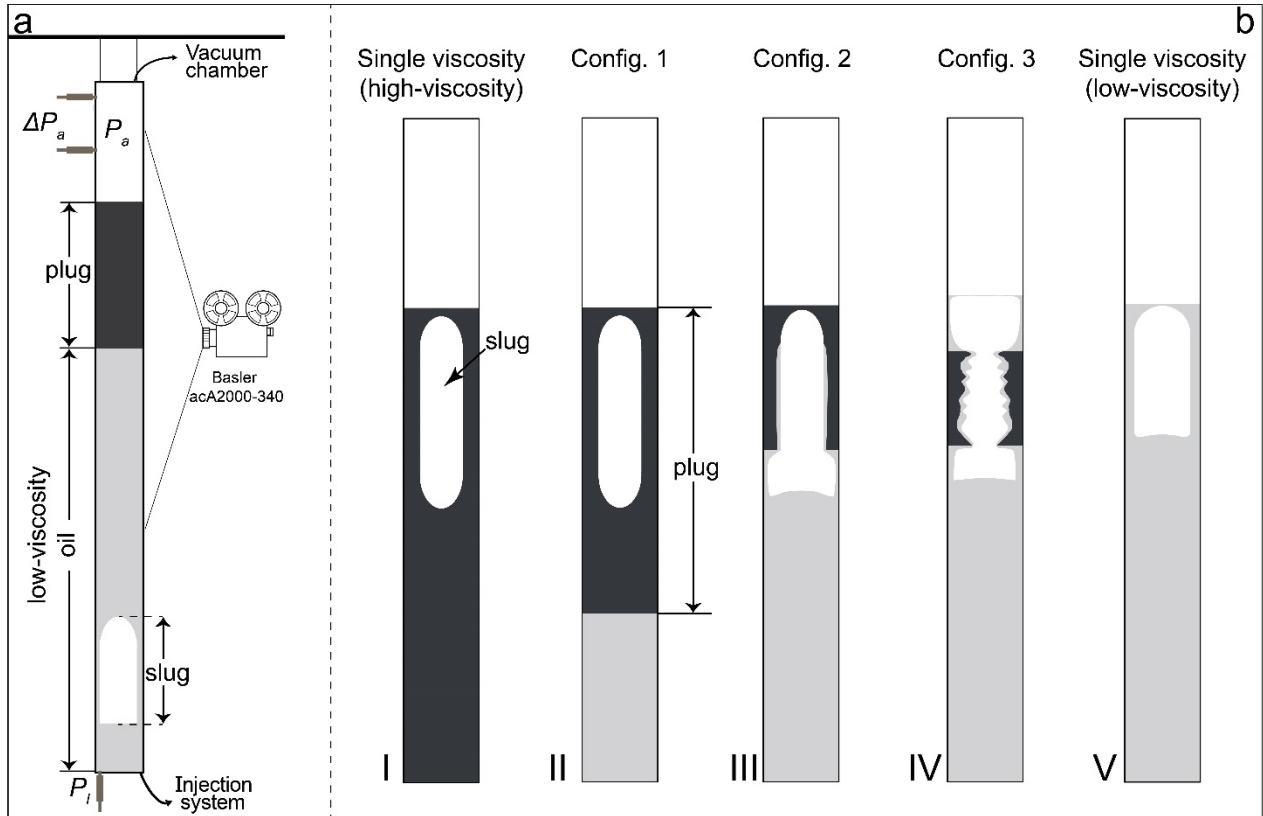
619   **Figure 3**

622 **Figure 4**

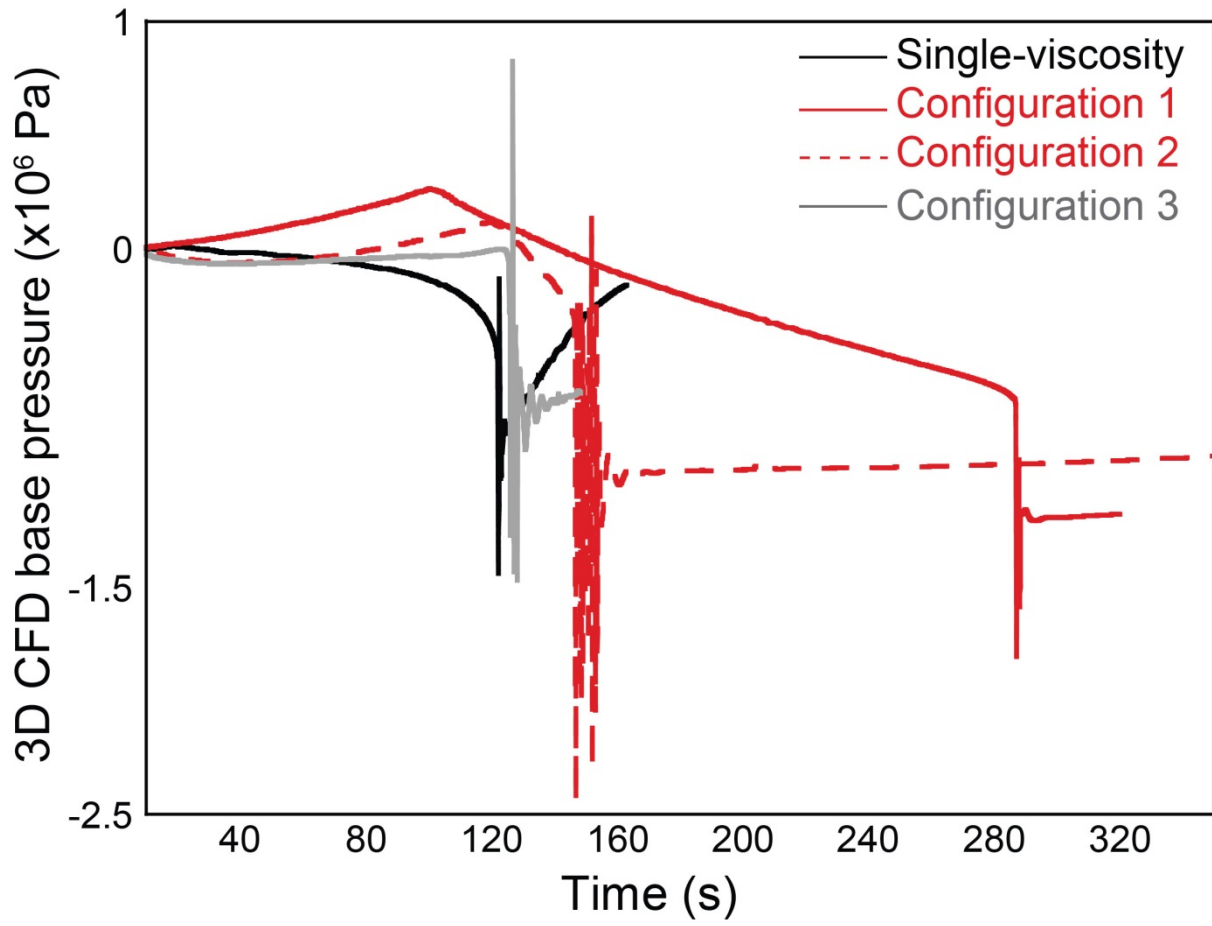625 **Figure 5**

628   **Figure 6**
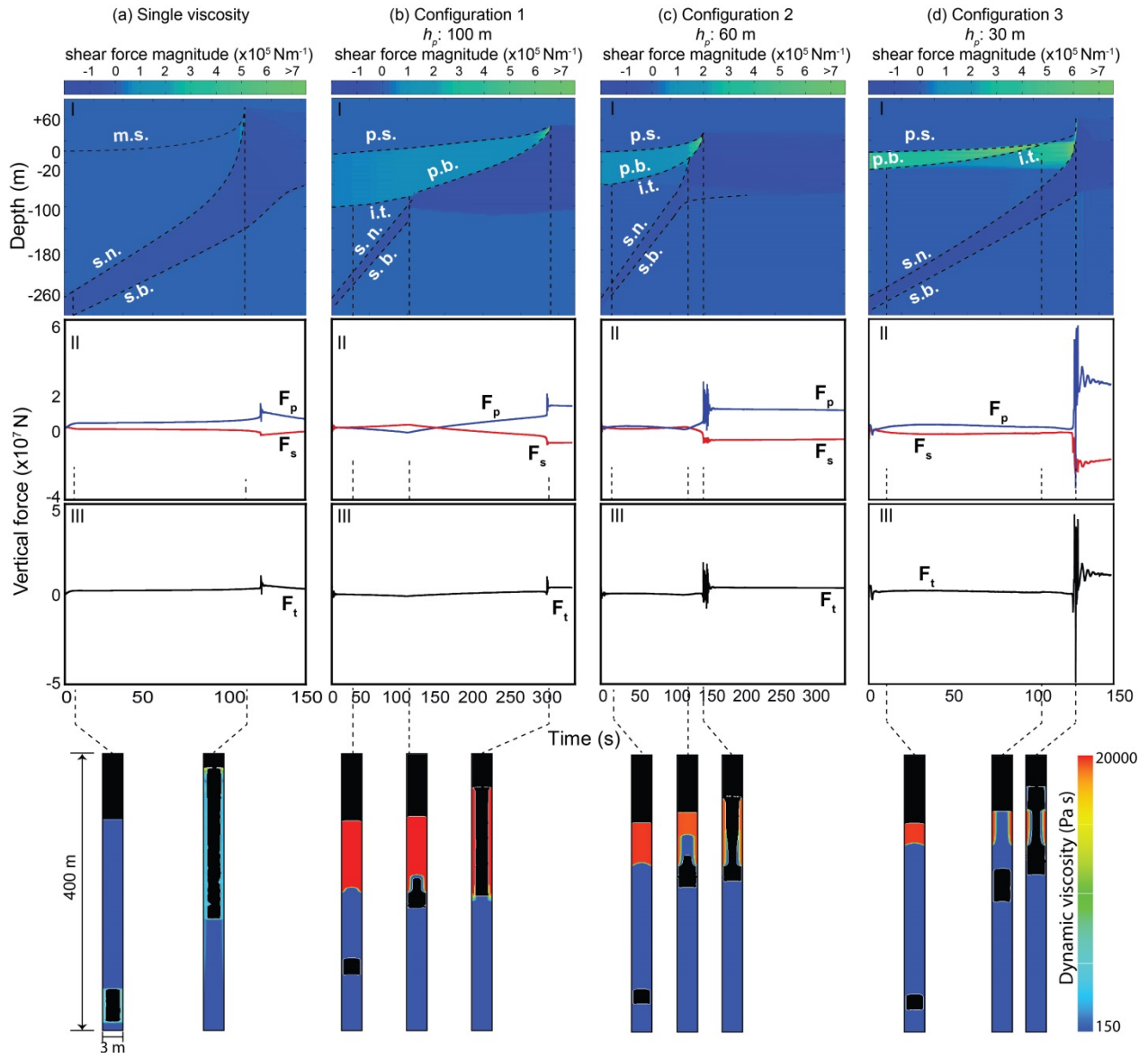

629

630

631   **Figure 7**

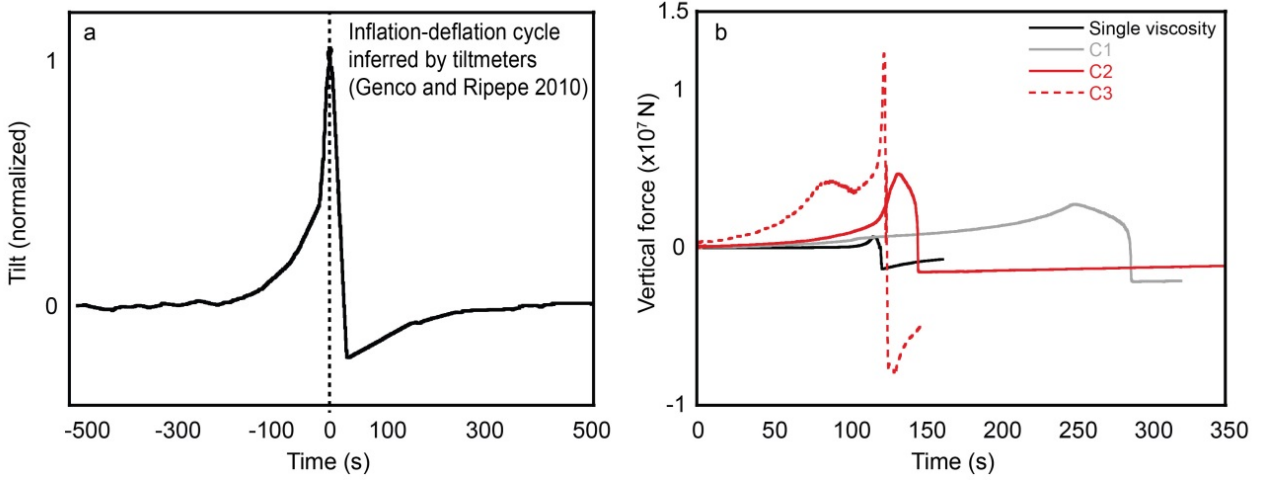

m.s. = magma surface   p.s. = plug surface   p.b. = plug base
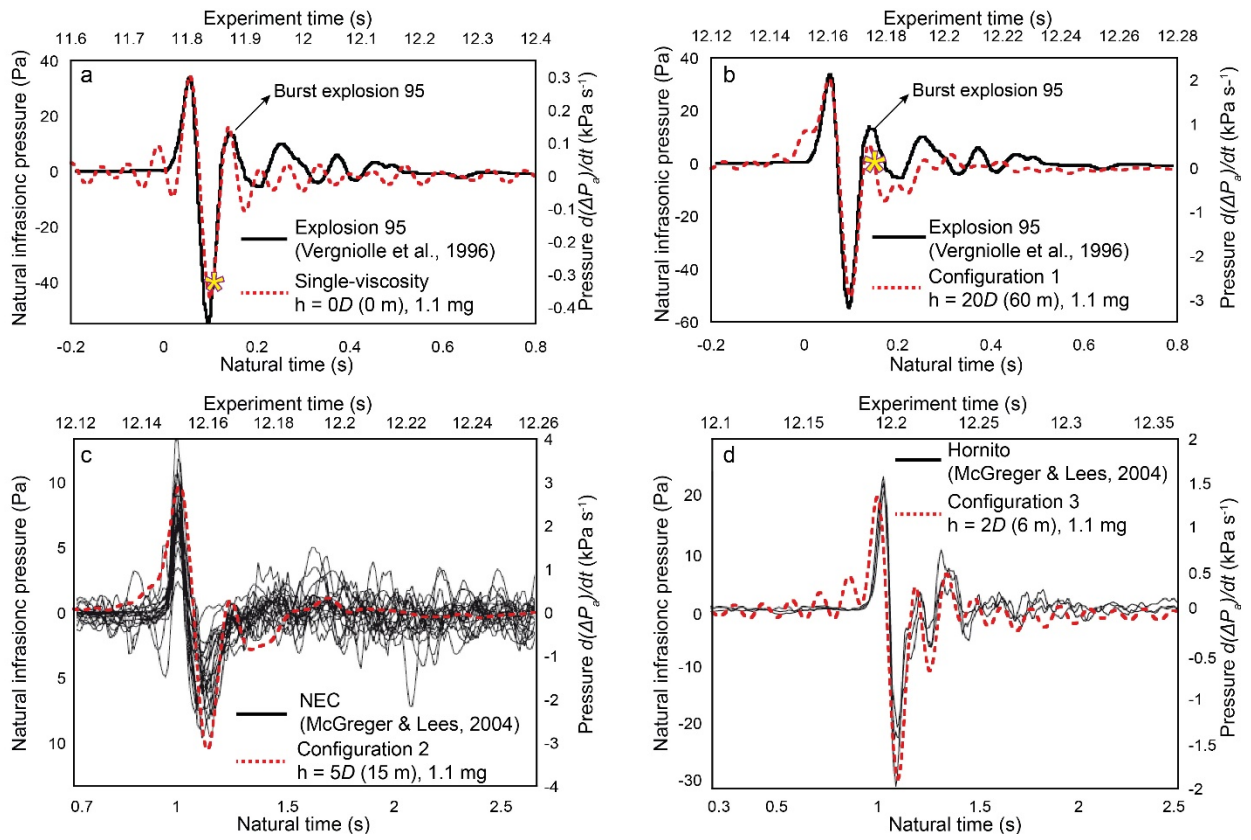s.n. = slug nose   s.b. = slug base   i.t. = intrusion top
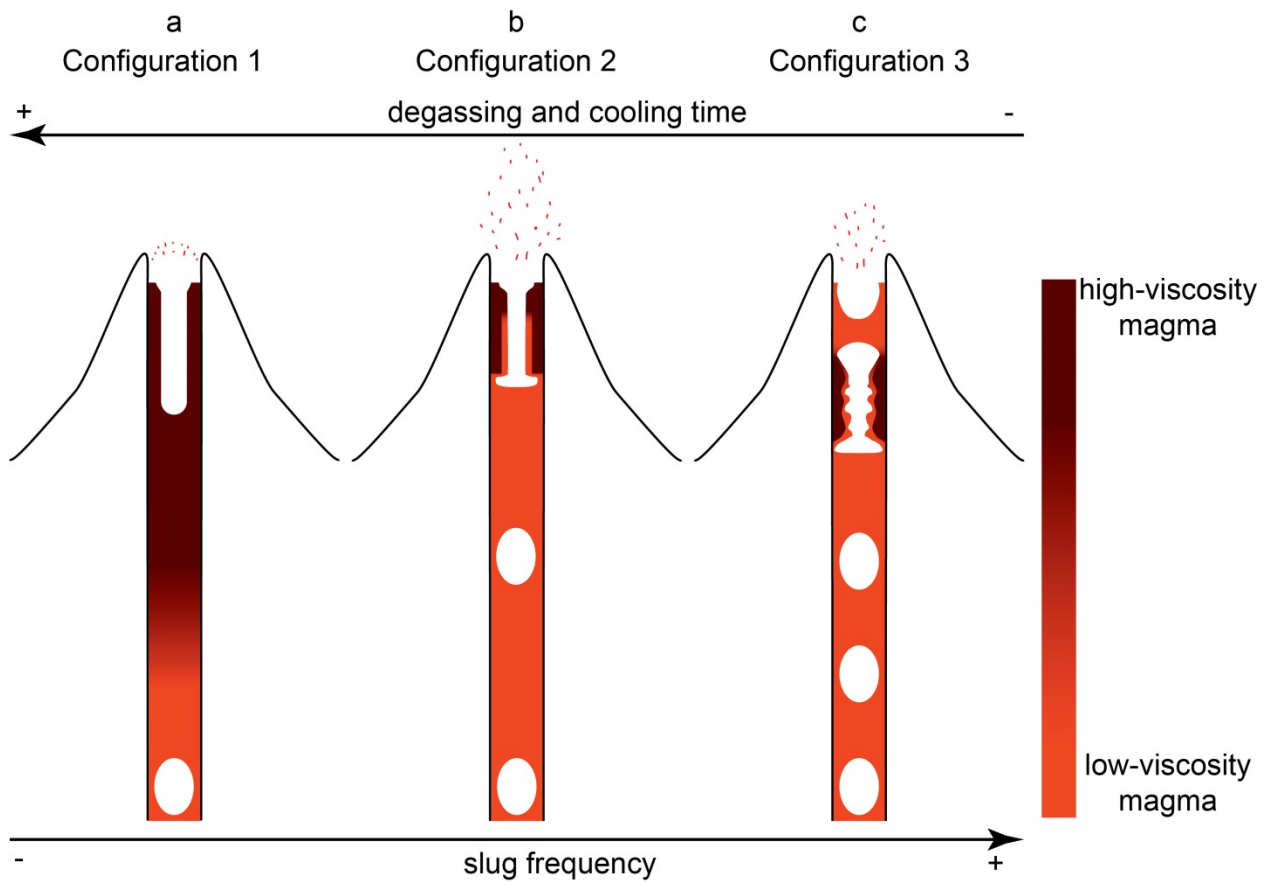
632

633

634   **Figure 8**

635

636

637   **Figure 9**

640 **Figure 10**

a
Configuration 1

b
Configuration 2

c
Configuration 3

+ degassing and cooling time -

high-viscosity magma

low-viscosity magma

- slug frequency +

641

642

Captions

Fig. 1. (**a**) The experimental apparatus comprised a 3-m-high vertical tube, with a diameter $D =$ 0.025 m, connected to a vacuum chamber, large in size relative to injected gas volume, and a gas injection system. Pressure variations were measured at 5 kHz (NI-PCI6034E data-logger), within the liquid at the bottom of the apparatus, by a BOC Edwards ASG2000 sensor (P_l), and above the liquid by two Honeywell differential pressure transducers 163PC01D75 (ΔP_a). Slug ascent, expansion and burst through the experimental liquids were imaged with a Basler high-speed camera acA2000-340km at 300 fps. (**b**) Conceptual sketches of tubes filled with (**I**) high-viscosity and (**V**) low-viscosity liquid representing end-member configurations that bracketed three main flow configurations. (**II**) In Configuration 1, the high-viscosity plug volume is sufficiently large to fully accommodate the gas slug. (**III**) In Configuration 2, a plug can accommodate the intrusion of low viscosity liquid, but not all the gas volume: the slug burst whilst within the plug with the slug base still in the low-viscosity liquid. (**IV**) In Configuration 3, slug expansion is sufficiently large to drive the low-viscosity intrusion through the plug, extruding a low-viscosity layer above the plug from which the slug burst (modified from Capponi et al., 2016a, with permission from Elsevier).

Fig. 2. Pressure within the liquid at the tube base (P_l) varies with flow process and time. (**a**) Sketches of the flow processes observed for each configuration (C1, C2, C3) as: (**I**) the slug ascended in the low-viscosity liquid beneath the plug, (**II**) as the slug nose entered the viscous annulus and (**III**) at burst. (**b**) Resulting pressure variations within the liquid (P_l) are shown for a 1.1 mg slug (6 ml) ($P_a = 1$ kPa) ascending through a single-viscosity system (black line), Configuration 1 (red line), Configuration 2 (dashed red line) and Configuration 3 (grey line). Note the greater maximum in P_l for Configuration 1 with respect to the single-viscosity control system, followed by decreasing pressure (**II**), developed during the transition of the slug from

667   within the low-viscosity liquid to within the plug and ending as soon as the entire slug length is

668   fully accommodated by the plug. The timing for the processes **II** and **III** differed between

669   configurations due to different plug thickness and variations in slug ascent mechanism within the

670   plug.

671   **Fig. 3.** Changes in gas pressure above the liquid for the single (low) viscosity system. (**a**) Peak

672   excess pressure $\Delta P^{\wedge}_a$ (black symbols) is reported as function of experimental gas masses (M).

673   Peak amplitudes of the time derivative of pressure variations $d(\Delta P_a)/dt$ (grey symbols) are also

674   reported. (**b**) Dimensionless ratio between theoretical slug overpressure at burst (ΔP_b) to

675   measured peak excess pressure ($\Delta P^{\wedge}_a$) plotted against the dimensionless slug stability index (γ)

676   for all the experimental masses (mg, black dots; $P_a = 1$ kPa). The transition between passive and

677   transitional regimes is identified by $\gamma = 1$ (for an empirical M = 0.9 mg or $V_0 = 4.85$ ml) and

678   between transitional and explosive regimes by the intersection of the linear empirical curves at γ

679   = 2.31, corresponding to M = 2 mg or V_0= 11.2 ml. Waveform shapes of (**c**) excess pressure

680   variations (ΔP_a) and (**d**) time derivative of pressure variations $d(\Delta P_a)/dt$, as function of time (P_a=

681   1 kPa) for   slug masses of 0.71 mg, 1.8 mg and 5.7 mg, are representative of the passive,

682   transitional and explosive regimes respectively. The insets in (**c**) and (**d**) show details of ΔP_a and

683    $d(\Delta P_a)/dt$ respectively, for the 4 ml slug. Error estimate due to variations in the mass of injected

684   gas, the experimental ambient pressure or sensor sensitivity is indicated in the bottom right

685   corner of each plot.

686   **Fig. 4**. (**a**) Peak excess pressure $\Delta P^{\wedge}_a$ normalised against P_a of 1 kPa shows, for the same plug

687   thickness, a dependence on gas mass M; (**b**) as a function of plug thickness (dimensionless), for

688   the same gas mass (colours) and varying plug thickness, $\Delta P^{\wedge}_a$ is dependent on the flow

689   configurations (symbols). The grey band identifies $\Delta P^{\wedge}_a$ for the single-viscosity system. Note in

690   **(b)** how larger M (4.3–9 mg or 17–49 ml) showed more variability in $\Delta P\hat{}_a$ within the same flow

691   configuration (Configuration 3) and for plug thickness of $1D$ (2.5 cm) and $2D$ (5 cm): this

692   configuration, for this range of volumes, promoted bubble breakup, generation of offspring slug

693   bubbles and partial blockages of the tube that strongly affected the gas release, leading to a

694   pulsatory release of the gas and caused variable impedance of gas escape rate from the bubble

695   (Del Bello et al., 2015; Capponi et al., 2016a). Error estimate due to variations in the mass of

696   injected gas, the experimental ambient pressure or sensors sensitivity is not given individually,

697   but is indicated in the bottom right corner of the plots.

698   **Fig. 5**. (**a**) Excess pressure variations (ΔP_a) and (**b**) time derivative of pressure variations,

699    $d(\Delta P_a)/dt$, as function of time for a 1.1 mg slug (6 ml) ($P_a = 1$ kPa) ascending through a single-

700   viscosity system (black line), C1 (grey line, $h_p = 50$ cm, $20D$), C2 (red line, $h_p = 12.5$ cm, $5D$)

701   and C3 (dashed red line, $h_p = 5$ cm, $1D$) show the dependence of pressure variations on flow

702   configurations. (**c**) Pressure variations above (ΔP_a, red line) and within (P_l, blue line) the liquid

703   and (**d**) time derivative of excess pressure variations $d(\Delta Pa)/dt$ as function of time for a 4.3 mg

704   ml (24 ml) slug and $P_a = 3$ kPa bursting in C3, showing the effect of highly variable gas release

705   rates during burst. The main atmospheric compressional pulse is followed by two secondary

706   pulses related to the burst of two offspring bubbles, interspaced by sub-pluses generated by

707   transient partial restriction of the slug pathway. Note a gradual decrease in the acoustic

708   amplitudes associated with the secondary pulses. For each secondary slug bubble, P_l showed

709   pressure drops while the system was already re-pressurizing as the oil film drained back to the

710   liquid surface following the main burst (**c**). These pressure drops share a similar waveform to the

711   one produced by the main burst, with a gradual decrease in magnitude; once all the bubbles

712   burst, the system continued re-pressurizing. The process is a pressurization-depressurization-

713 repressurization sequence, with duration a function of the total number of secondary slug

714 bubbles.

715 **Fig. 6.** Basal fluid pressure variation derived from 3D CFD simulations at volcanic scale for a

716 400-m-high volcanic conduit of radius 1.5 m, and a slug of initial gas volume $V_0 = 158$ m^3

717 (equivalent to 440 kg) ascending through a single-viscosity system (black line, height of magma

718 $h_m = 300$ m, viscosity $\mu = 150$ Pa s), C1 (red line, $h_m = 200$ m, plug height $h_p = 100$ m, plug $\mu =$

719 20 kPa s), C2 (dashed red line, $h_m = 240$ m, $h_p = 60$ m) and C3 (grey line, $h_m = 270$ m, $h_p = 30$ m).

720 Model pressures are relative to static at the base of the magma column to facilitate direct

721 comparison and give a clearer overview of pressure increases and decreases.

722 **Fig. 7.** Results from 3D simulations in which a slug of initial gas volume $V_0 = 158$ m^3, equivalent

723 to a gas mass of 440 kg, ascends in a 400-m-high volcanic conduit filled with (**a**) a magma

724 column of viscosity $\mu = 150$ Pa s (Single-viscosity), and with a low-viscosity magma ($\mu = 150$ Pa

725 s) overlaid by a more viscous plug ($\mu = 20$ kPa s) of (**b**) height $h_p = 100$ m (Configuration 1), (**c**)

726 $h_p = 60$ m (Configuration 2) and (**d**) $h_p = 30$ m (Configuration 3). In **I**, we plotted the magnitude

727 of the vertical shear acting on the conduit over the time. In **II**, the vertical force exerted on the

728 volcanic conduit by liquid shear (F_s) and the vertical force due to pressure variations at the base

729 of the conduit (F_p) are shown. The net force, $F_t = F_s + F_p$, is plotted in **III**. The vertical cross-

730 section snapshot images show the conduit processes in the simulations at the time indicated by

731 the vertical dashed lines; the colours indicate the magma viscosity.

732 **Fig. 8. (a)** Cycle of inflation-deflation inferred by tiltmeters at Stromboli, reproduced from

733 Genco and Ripepe (2010, with permission from AGU) showing an initial pre-burst ground

734 inflation lasting ~200 s, often up to ~500 s, that accelerates ~20-30 s before burst. The onset of

735 the explosive event (black dashed line at $t = 0$) coincides with the end of the inflation, followed

736   by a rapid downward tilt deflation. (**b**) Vertical force exerted by liquid shear isolated from the

737   3D CFD simulation shown in Fig. 6, for the section of the volcanic conduit between the initial

738   magma free-surface (-100 m) up to burst point for a single viscosity system (-57 m, black line),

739   C1 (-73 m, grey line), C2 (-80 m, red line) and C3 (-68 m, red dashed line). Note the different

740   timescales and force magnitudes between the single-viscosity system and the flow

741   configurations.

742   **Fig. 9.** The time derivative $d(\Delta Pa)/dt$ for an experimental 6 ml (1.1 mg) slug ascending through

743   (**a**) single low-viscosity system, (**b**) C1, (**c**) C2, and (**d**) C3, was compared to infrasonic signals

744   measured at Stromboli from (**a**, **b**) Vergniolle et al. (1996, reproduced with permission from

745   AGU) and from (**c**, **d**) McGreger and Lees (2004, reprinted with permission from Elsevier). Both

746   time and pressure axis were scaled by the same factor to best fit the experimental to the

747   measured data. The asterisk in (**a**) and (**b**) indicated the burst point of the 6 ml experiment. Note

748   that high frequency oscillations emerge calculating $d(\Delta Pa)/dt$, in particular for (**a**) and (**d**),

749   plausibly representing resonance of the gas within the experimental tube. Note that we are

750   referring to signals specific for a given activity at that given vent at a specific time. Activity at

751   Stromboli is highly variable, with vents shifting in position, size and activity at timescales from

752   hours to years, therefore no single signal can be considered representative of one vent at all

753   times.

754   **Fig. 10.** Conceptual sketches illustrating the possible effect of slug frequency on conduit

755   dynamics. (**a**) For a slow frequency, the time interval between explosions may be large enough

756   to allow the generation of a degassed and viscous layer of magma at the top of the conduit, large

757   enough to accommodate the ascending slug. The quiescent time preceding the next explosion

758   may allow the viscous layer to settle again. (**b**) An increase in the slug frequency could reduce

759   the cooling time of the magma, and, as result, the thickness of a possible viscous layer may be

760   reduced as well. If reduced enough, the plug will not be large enough to accommodate both the

761   liquid intrusion and the ascending slug. The slug will then burst in the plug, with its base still in

762   the low-viscosity magma. (**c**) Higher-frequency could create an open path right through the plug,

763   kept open by the train of ascending slugs. Each time a slug passes through the geometrical

764   discontinuities, the slug break-up process may be triggered, and instabilities along the liquid film

765   may create partial blockages of the slug path, resulting in longer and complex eruption and

766   highly variable gas release rates.